High-resolution neutron transmission and capture measurements of the nucleus ^{206}Pb

A. Borella,[1] F. Gunsing,[2] M. Moxon,[3] P. Schillebeeckx,[1,*] and P. Siegler[1]
[1] *EC-JRC-IRMM, Retieseweg 111, B-2440 Geel, Belgium*
[2] *CEA/Saclay, DSM/DAPNIA/SPhN, F-91911 Gif-sur-Yvette, France*
[3] *Hyde Copse 3, Marcham, United Kingdom*
(Received 2 April 2007; published 9 July 2007; corrected 11 July 2007)

Neutron total and capture reaction cross-section measurements for ^{206}Pb were performed at the GELINA neutron time-of-flight facility in the energy range from 1 to 620 keV. The resonance parameters corresponding to 304 excited nuclear levels in ^{207}Pb were determined from the data using the R-matrix formalism. The results are compared to existing data. From the capture data photon strength functions have been deduced. No evidence has been found for a previously reported enhancement of the $M1$ transition strength, nor for a strong enhancement of the s-wave doorway state in the photon channel. The neutron capture cross section of ^{206}Pb is of importance in stellar evolution calculations of the formation of the elements by neutron capture. Maxwellian-averaged neutron capture cross sections have been calculated at different stellar temperatures ranging up to 100 keV and compared with the results of previous work and evaluated data libraries.

DOI: 10.1103/PhysRevC.76.014605 PACS number(s): 25.40.Lw, 25.40.Ny, 27.80.+w, 28.20.Fc

I. INTRODUCTION

Resonance parameters for neutron-induced reactions on Pb isotopes are important for the understanding of stellar nuclear synthesis, for studies of neutron-induced reaction mechanisms, and for the design of spallation neutron sources.

Capture cross-section data for Pb isotopes are required in stellar codes for a quantitative assessment of the nuclear synthesis via the s-process. For a reliable analysis, s-process abundances should be predicted with an accuracy of about 5% [1]. According to a sensitivity study in the Pb/Bi region performed by Ratzel *et al.* [1], such an accuracy implies a 5% uncertainty level on the Maxwellian-averaged capture (MAC) cross section for ^{206}Pb. The lack of accurate capture cross section data for ^{206}Pb can be noted in the most recent compilation of MAC cross sections by Bao *et al.* [2]. The MAC cross sections at a thermal energy $kT = 30$ keV that they deduced from the data in Refs. [3–5] fluctuate by more than 5%.

One of the most promising concepts of a neutron source for Accelerator Driven Systems (ADS) is based on the use of a lead-bismuth eutectic core as spallation target, coolant, and moderator. To optimize the design and carry out a safety assessment of such systems, nuclear data for neutron-induced reactions for Pb and Bi play an important role. Broeders *et al.* [6] investigated the incineration of Pu in ADS with Th-based fuel. A study of the k_{eff} as a function of the burn-up indicated discrepancies in the cross-section data for the lead isotopes. The k_{eff} differed by about 0.3% using the cross-section data for $^{\mathrm{nat}}$Pb compared to the value obtained from the data of the individual Pb isotopes and differences of up to almost 1% were obtained when using cross-section data from the various libraries. A sensitivity analysis of neutron cross-section data relevant for ADS in Ref. [7] indicated a discrepancy of 12% between the ^{206}Pb(n, γ) reaction rates obtained with data from JENDL 3.3 and ENDF/B-VI.8.

For most applications nuclear model systematics are required to predict cross sections in regions were no experimental data are available. Systematics of level densities, γ and neutron strength functions are important input parameters for theoretical calculations of nuclear reactions. These quantities can be obtained from resonance parameters deduced from high-resolution reaction cross-section measurements in the resolved resonance region. The data library RIPL2 [8] contains a major compilation of them.

Resonance parameters for neutron induced reactions for ^{206}Pb in the evaluated data libraries are mainly based on the work of Refs. [3–5,9,10]. Horen *et al.* [9,10] deduced the resonance energy, neutron width, spin, and parity of the resonances from their transmission and elastic-scattering data measured at the ORELA time-of-flight facility. These measurements were carried out on samples of radiogenic lead (88.38% enriched in ^{206}Pb). To compensate for the ^{207,208}Pb content in the sample, a combination of a natural lead sample and a lead sample enriched to 92.4% in ^{207}Pb was used for the sample out measurements. The capture measurements of Allen *et al.* [3], Mizumoto *et al.* [4] and Musgrove and Macklin [5] have also been carried out at ORELA. Mizumoto *et al.* [4] and Allen *et al.* [3] used the same setup consisting of C_6F_6 detectors in a 90° geometry and a radiogenic sample (88.38% enriched in ^{206}Pb). Although a 3 and 10% normalization uncertainty were quoted in Refs. [4] and [3], respectively, the capture area for the first p-wave resonance at 3.36 keV differed by more than a factor of 2. The experimental conditions and results of the measurements performed by Musgrove and Macklin [5] are accessible only through the EXFOR database [11]. More recently, a capture measurement has been performed at the n_TOF facility at CERN [12].

It can be concluded that the experimental capture cross-section data for ^{206}Pb do not meet the required accuracy. To improve the experimental data for neutron-induced reactions

*peter.schillebeeckx@ec.europa.eu

of ^{206}Pb within the requested uncertainty level, high-resolution total and capture cross-section measurements were performed at GELINA using metallic lead samples enriched in ^{206}Pb. In addition, measurement conditions and analysis procedures, as described in Ref. [13], were implemented to reduce as much as possible bias effects due to the weighting function, normalization, angular correlation effects, and neutron sensitivity of the capture detection system.

This work is part of a PhD thesis [14].

II. EXPERIMENTAL METHOD

The experiments were carried out at the neutron time-of-flight facility GELINA of the Institute for Reference Materials and Measurements (IRMM), Geel, Belgium. A detailed description of the accelerator and its neutron producing target can be found in Ref. [15]. The accelerator was operated at 800 Hz with a 70-μA average electron current, providing electron pulses with 100 MeV average electron energy and 1-ns pulse width. This short burst width was obtained with a pulse compressing magnet system [16]. High-energy electrons generate Bremsstrahlung in a mercury-cooled rotating uranium target, where neutrons are produced by (γ, n) and (γ, f) reactions. Two water-filled 4-cm-thick Be containers were used to moderate the fast neutrons and to increase the neutron flux in the region below a few hundred keV. For both transmission and capture measurements a shadow bar made of Pb and Cu was placed close to the uranium target to reduce the γ-ray flash and the fast neutron component. The samples for the transmission and capture experiments were made from a batch of metallic lead enriched to 99.82% in ^{206}Pb, on loan from Oak Ridge National Laboratory. The isotopic composition, which is given in Table I, and impurities of the metallic lead were verified by prompt γ-ray activation analysis at the cold neutron source of the Budapest Neutron Centre [14]. Only γ rays resulting from thermal neutron capture on ^{207}Pb(n, γ) were observed, corresponding to a 0.2 at% relative amount of ^{207}Pb, and no other impurities were identified.

TABLE I. The isotopic composition of the enriched ^{206}Pb samples used for the transmission and capture measurements.

Isotope	Atomic percentage
^{204}Pb	<0.01
^{206}Pb	99.82 ± 0.03
^{207}Pb	0.16 ± 0.02
^{208}Pb	0.02 ± 0.01

A. Transmission measurements

The transmission measurements were performed at a 26-m flight path of GELINA, forming an angle of 99° with the direction of the electron beam, on two 20 × 20 mm metallic ^{206}Pb samples with a thickness of 0.0160 and 0.0300 atoms/b. The experimental arrangement is shown in Fig. 1. The moderated neutron beam was collimated by several annular collimators within an evacuated beam pipe. The sample changer was placed at a diestance of 9 m from the neutron-producing target behind a 294-mm-long collimator, made up of Li-carbonate plus resin and Cu. The aperture of the last Cu collimator resulted in a 15-mm-diameter neutron beam at the sample position. Almost halfway between the neutron target and the sample position, a sample changer for permanent (^{10}B and S) and black resonance filters was installed. A 0.013-atoms/b-thick ^{10}B antioverlap filter was used to eliminate the effect of overlap neutrons from previous accelerator cycles and a 115-mm-thick sulfur filter was installed to reduce the influence of the in-beam γ rays

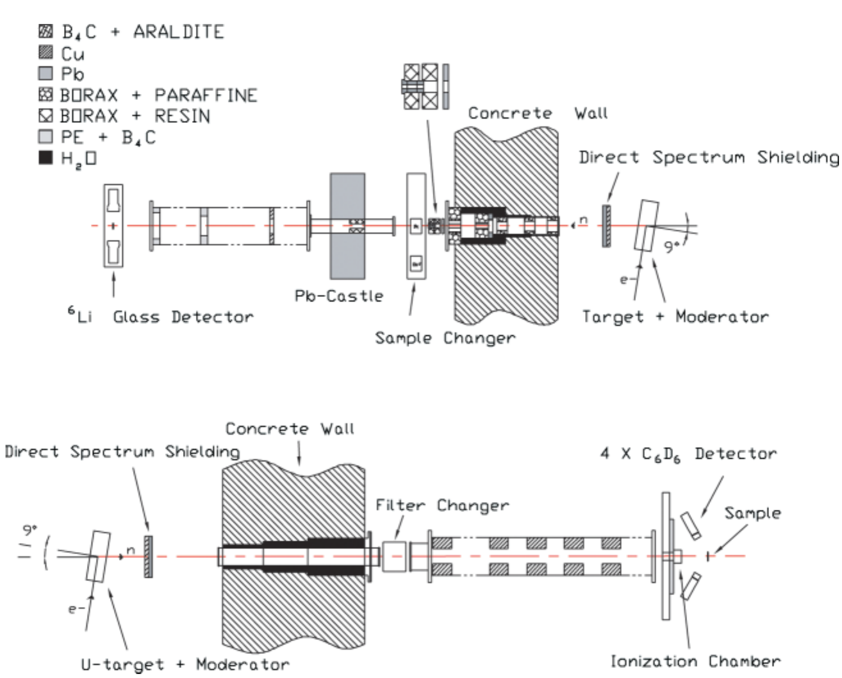

FIG. 1. (Color online) Experimental arrangement for the transmission (above) and the capture (below) measurements performed at the GELINA neutron time-of-flight facility.

and to continuously monitor the background at 102.7 keV. Additional measurements with other black resonance filters were performed to deduce the contribution of the time-dependent background. Downstream the filters and the sample, the neutron beam was further collimated and finally detected by an NE912 Li-glass scintillator enriched to 95% in ^{6}Li, which was placed at 26.45 m from the neutron-producing target. The Li glass, with a 110-mm effective diameter and 12.7-mm thickness, was placed in an Al canning and viewed by two EMI9823QKB photomultipliers (PMT), placed perpendicularly to the neutron beam axis. Air-conditioning was installed at the measurement station to reduce electronic drifts due to temperature changes and to keep the sample at a constant temperature. The temperature at the sample position was continuously monitored. The average temperature was then used in the resonance shape analysis program to calculate the Doppler broadening of the resonances. The dead time of the detection chain was monitored continuously by registering the time-interval distribution between adjacent events. The resulting dead time was 1160 ns.

In transmission measurements the observed quantity is the fraction of the neutron beam that passes through the sample without any interaction. The transmission factor $T_{\rm exp}$ is obtained from the ratio of a sample-in measurement $C_{\rm in}$ and a sample-out measurement $C_{\rm out}$, both corrected for their dead-time effects and background contributions:

$$T_{\rm exp}(T_n) = N_T \frac{C_{\rm in}(T_n)}{C_{\rm out}(T_n)}, \tag{1}$$

where T_n is the time-of-flight of the neutron. The normalization constant N_T accounts for the ratio of the integrated intensities of the incident neutron beam during the "in" and "out" cycles of the sample. Two BF_3 proportional counters, placed at different locations around the target hall, were used to monitor the total neutron output of the accelerator and to deduce the normalization factor N_T. To avoid systematic uncertainties due to slow variations of the beam profile and/or detector efficiency as a function of time, alternating sequences of "in-out" measurements of about 30 min were carried out. Such a procedure reduces the uncertainty on the normalization factor N_T to less than 0.5%. The background was derived from the counts observed in the minima of the saturated resonance dips formed by the so-called black resonances of Co, Bi, Na, and S filters, which remove all neutrons at 132 eV, 800 eV, 2.85 keV, and 102.7 keV, respectively. The signal-to-background ratio was 50:1 at 132 eV, 40:1 at 800 eV, 30:1 at 2.85 keV, and 20:1 at 102.7 keV. The background over the whole time range was approximated by a power function, including a constant term.

B. Capture measurements

The capture measurements were performed at a 58 m measurement station on a 60-mm-diameter × 1.08-mm-thick metallic disk, corresponding to 3.546×10^{-3} atoms/b of ^{206}Pb. A vertical cross section of the experimental setup is shown in Fig. 1. The angle between the flight path and the direction of the electron beam was -81°. Just outside the 3-m-thick bunker wall, a 0.042-atoms/b-thick ^{10}B permanent overlap filter was installed together with a sample changer for black resonance filters. The moderated neutron beam was collimated to about 75 mm in diameter at the sample position. An air-conditioning system was installed to keep the sample at a constant temperature and to reduce electronic drifts.

The γ rays originating from the capture reaction in the sample were detected by four NE230 cylindric C_6D_6 liquid scintillators (10 cm in diameter and 7.5 cm in thickness) that were oriented at 125° with respect to the direction of the incoming neutrons. This geometry was chosen to minimize systematic effects due to the anisotropy in the primary dipole γ-ray emission from resonances with a spin $J > 1/2$ and an orbital angular momentum $\ell > 0$. This avoids correction procedures that require the knowledge of the γ-ray cascade after neutron capture. In an attempt to reduce the detection of scattered neutrons to a minimum, each scintillator was coupled to an EMI9823QKB quartz-windowed PMT. For each detector the anode signal from the PMT was used to determine the arrival time of the neutron and the signal of the ninth dynode to provide information about the energy E_d deposited by the γ-ray in the C_6D_6 detector. The discrimination level of the capture detection system corresponded to 150 keV deposited energy.

The pulse-height weighting technique was applied to the detector output pulses to allow for a detection efficiency of a capture event being proportional to the total γ-ray energy emitted when a neutron is captured. Monte Carlo simulations were used to obtain the weighting functions for the ^{206}Pb(n,γ) data. The weighting function was defined for a finite discriminator level of $E_d = 150$ keV. Such a weighting function directly accounts for the missing contribution of γ rays depositing less than E_d in the detector and avoids a correction procedure for this missing part that requires information about the γ-ray emission spectrum [13]. Because the macroscopic total cross section for the ^{206}Pb sample was small, it was assumed that the γ rays for the ^{206}Pb(n,γ) measurements were produced uniformly across the sample and no correction to the γ rays for the attenuation of the neutrons was applied. Because the lowest γ-ray energy in neutron capture by ^{206}Pb is 570 keV, no correction for internal conversion was required. Due to the low detection efficiency the probability of coincident events was below 1%. As explained by Wilson *et al*. [17] the impact of these events can be neglected.

The shape of the neutron flux below 150 keV was continuously measured with a ^{10}B ionisation chamber placed 80 cm before the sample. For neutron energies above 150 keV additional measurements with a ^{235}U fission chamber were performed. The ^{10}B chamber was a Frisch gridded ionization chamber with three back-to-back layers of ^{10}B evaporated on a 30-μm-thick aluminium backing, with a total thickness of about 1.25×10^{-5} atoms/b ^{10}B and a diameter of 84 mm. The ^{235}U fission chamber was a parallel plate chamber with a single 100-mm-diameter layer of 2.53×10^{-6} atoms/b ^{235}U, which was evaporated on a thin aluminium backing. Both chambers were operated with a continuous flow of a mixture of argon (90%) and methane (10%) at atmospheric pressure.

The shape of the neutron flux (in units of lethargy) as a function of neutron energy is shown in Fig. 2. This figure illustrates the good agreement between the shape

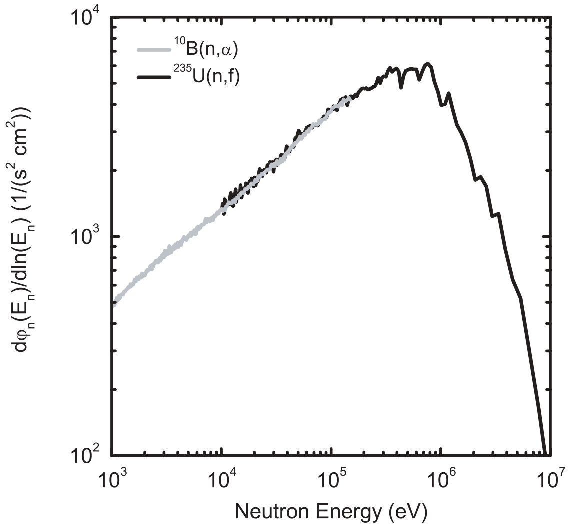

FIG. 2. The neutron spectrum at the 58-m capture station, obtained from ^{10}B(n,α) and ^{235}U(n,f) measurements, with the accelerator operating at 800 Hz.

obtained from the ^{10}B(n,α) and ^{235}U(n,f) measurements. The uncertainties for the ^{10}B(n,α_1) cross section from thermal to 150 keV is between 0.2 and 1.5% [18] and the uncertainty for the ^{235}U(n,f) cross section between 150 and 600 keV is 1.5% [19]. Based on these values it is assumed that the capture data have an uncertainty of 1.5% related to the determination of the incident neutron flux shape.

The time-of-flight and the pulse height of each detected event were recorded sequentially in list mode. This allowed a continuous stability check of the detection systems and an off-line application of the weighting function. The stability of both the detection systems and the accelerator operating conditions (i.e., frequency, current, and neutron output) were verified in cycles of 1 h. The linearity and resolution of the C_6D_6 detectors were monitored on a weekly basis by measurements of the 661.7 keV and 6.13 MeV γ-ray using a ^{137}Cs and a ^{238}Pu+^{13}C source, respectively. In addition, the 2.2 MeV γ-ray from the H(n,γ) reaction, which was present as a background contribution, was used for an off-line adjustment of the gain. The dead time of the capture and neutron detection chains were monitored continuously by registering the distribution of the time-of-flight differences between consecutive events. For the flux measurements the dead time was 4180 ns, with a maximum dead-time loss of 0.2%. The dead time of 5330 ns for the capture measurements resulted in a 0.4% maximum dead-time correction.

The fraction of neutrons interacting in the sample and creating a signal in the detection system is observed in capture measurements. This fraction, i.e., the yield Y_{exp}, is obtained from the ratio of the counts seen by the capture detector and the incident neutron flux φ_n:

$$Y_{\text{exp}}(T_n) = \frac{C_w(T_n) - B_w(T_n)}{\varphi_n(T_n)}, \tag{2}$$

where C_w and B_w are the observed dead-time corrected weighted count rates of the sample and background measurement, respectively. The background contribution B_w can be assessed by additional measurements or approximated by an analytical expression. Because of the very low capture cross section between the resonances this background component was determined using the resonance shape fitting program REFIT described later.

III. DATA REDUCTION AND ANALYSIS

The AGS code [20] was used to derive the transmission factor defined by Eq. (1) and the experimental yield given in Eq. (2) from the raw time-of-flight spectra. This package includes the most important spectra manipulations, such as dead-time correction, background fitting and subtraction, and normalization. The code performs the full propagation of covariance matrix starting from the uncorrelated uncertainties due to counting statistics.

To parametrize the data in terms of resonance parameters the resonance shape analysis code REFIT was used [21]. This code is based on the Reich-Moore approximation of the R-matrix formalism and accounts for self-shielding, multiple-scattering and Doppler effects, the resolution of the time-of-flight spectrometer, and the neutron sensitivity of the capture detection system. The code accommodates both numerical and analytical resolution functions adapted to a time-of-flight facility such as GELINA. A detailed description of the resolution function for time-of-flight measurements carried out at GELINA, including the results of Monte Carlo simulations performed by Coceva that were used in this work, can be found in Refs. [22] and [15]. The REFIT code also includes a procedure to correct for the influence of the neutron attenuation in the sample on the weighted response of a capture measurement as described in Ref. [13]. The code does not treat full covariance information on the experimental data and uses only the diagonal term. Therefore, the AGS code was used to quantify the correlated and uncorrelated uncertainty components on the transmission factor and experimental yield. Without accounting for the uncertainty component due to normalization factors and the shape of the neutron flux for the capture data, the maximum relative contribution of the correlated component on both the transmission factor and the experimental yield was less than 5%. Consequently, the largest correlated uncertainty component is due to the normalization factors and shape of the neutron flux. This contribution was not given in the resonance analysis and is quoted separately.

In the REFIT code the experimental transmission T_{exp} is expressed as a function of the total cross section σ_t and the sample thickness n in atoms per barn by:

$$T_{\text{exp}}(T_n) = \int R_{\text{T}}(T_n, E_n) e^{-n\sigma_t(E_n)} dE_n, \tag{3}$$

where $R_{\text{T}}(T_n, E_n)$ is due to the resolution of the time-of-flight spectrometer and expresses the probability that a neutron with an energy E_n will result in an event at time T_n. The experimental yield Y_{exp} obtained from capture measurements is expressed as a function of the theoretical capture yield Y_c

and scattering yield Y_n [13,21]:

$$Y_{\exp}(T_n) = N_c \int R_T(T_n, E_n)[\epsilon_{cw}(E_n)Y_c(E_n) + \epsilon_{nw}(E_n)Y_n(E_n)]dE_n, \quad (4)$$

where N_c is a normalization factor. The efficiency of the weighted response to detect a capture event or a scattered neutron is denoted by ϵ_{cw} and ϵ_{nw}, respectively. Neglecting the internal conversion process, the detection efficiency ϵ_{cw} is directly proportional to the total excitation energy, which is the sum of the neutron binding energy and the neutron energy in the center-of-mass system. The efficiency ϵ_{nw} is the probability that a scattered neutron creates a detectable signal. The second component, denoted by Y_{bn}, originates from neutrons that are scattered in the sample and subsequently captured in the detector environment:

$$Y_{bn}(T_n) = N_c \int R_T(T_n, E_n)\epsilon_{nw}(E_n)Y_n(E_n)dE_n. \quad (5)$$

For a nonfissionable nucleus and energies below the first inelastic scattering level, the capture and scattering yield are expressed as a function of the total (σ_t), capture (σ_γ), and scattering (σ_n) cross section by:

$$Y_c(E_n) = (1 - e^{-n\sigma_t})\frac{\sigma_\gamma}{\sigma_t} + Y_M \quad (6)$$

and

$$Y_n(E_n) = (1 - e^{-n\sigma_t})\frac{\sigma_n}{\sigma_t} - Y_M, \quad (7)$$

where Y_M accounts for the contribution of capture events after at least one neutron scattering in the sample. Full analytical expressions for both the capture and scattering yield, which are also valid for fissionable nuclei, are implemented in the REFIT code and can be found in Ref. [21]. A more detailed discussion on the calculation, validation, and application of the weighting function and the neutron sensitivity of the detection system can be found in Ref. [13].

The position of the γ-ray flash was used to deduce the zero point of the time scale with an uncertainty of 1 ns and the overall time resolution due to the electron burst and the detection chain. The effective flight path length of the capture setup 58.576 ± 0.002 m was deduced from an analysis of the 58.771- and 129.19-eV resonances obtained from ^{232}Th(n, γ) measurements in the same geometry. These energies were determined previously relative to ^{238}U from transmission measurements at a 50-m station of GELINA [23]. The flight path length of the transmission setup 26.452 ± 0.001 m resulted from a simultaneous analysis of the ^{206}Pb capture and transmission data. The normalization factor N_c for the capture data was determined from measurements on ^{nat}Fe samples and sandwiched samples of ^{nat}Fe-^{nat}Pb and ^{nat}Fe-^{206}Pb, using the 1.15-keV resonance of ^{56}Fe as a reference [24]. The resonance shape analysis was performed in the region around the 1.15-keV resonance, fitting only the normalization and background level and assuming a neutron width $\Gamma_n = 61.7$ meV and a radiation width $\Gamma_\gamma = 574$ meV. The final normalization factor based on the average value from the three samples agreed within 0.6% with the value obtained from measurements with

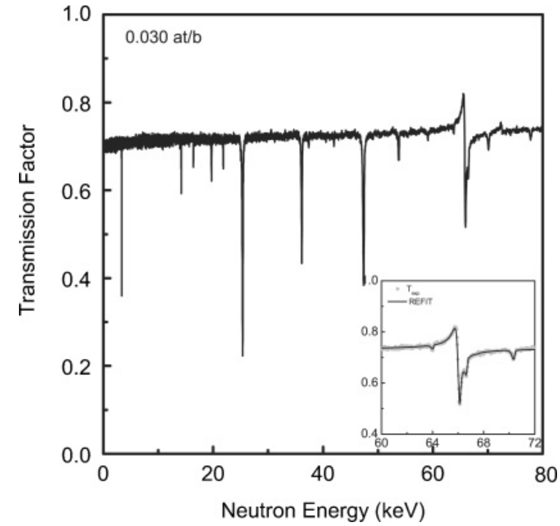

FIG. 3. The transmission factor for the 0.030-atoms/b-thick sample. The insert shows the result of an analysis with REFIT around the s-wave resonance at 66 keV.

a ^{nat}Ag sample using the saturated resonance at 5.2 eV. For the ^{nat}Ag(n, γ) measurements the accelerator was operated at 100 Hz.

IV. RESULTS

A. Total cross-section data

With the available amount of material the resonance energy and $g\Gamma_n$ values for the 17 most intense resonances up to 80 keV were determined from the transmission data. The quantity $g = (2J + 1)/2(2I + 1)$ is the statistical factor for a total angular momentum J and target spin I. The effective scattering radius R' for s-wave neutrons was fitted from the asymmetric pattern arising from the interference between potential and resonance scattering of the 16.43- and 66.00-keV s-wave resonances, as illustrated in Fig. 3. In the analysis the distant level parameter R^∞ was set to zero. The resulting radius $R' = 9.54 \pm 0.02$ fm deviates from the value $R' = 8.04$ fm used by Horen *et al.* [9]. Our value is in good agreement with the value $R' = 9.46 \pm 0.15$ fm adopted by Mughabghab [25]. The low uncertainty on the scattering radius deduced in this work is primarily due to the use of an isotopically pure ^{206}Pb sample and the good resolution of the time-of-flight spectrometer. From a simultaneous analysis of the thin and thick sample data the statistical factors for the strong resonances at 25.4, 36.2, and 47.5 keV were confirmed [14]. In Ref. [26] the results deduced from an analysis of the transmission data are compared with those reported by Horen *et al.* [9] and Mizumoto *et al.* [4]. A comparison with the data of Mizumoto *et al.* [4] shows deviations of up to a factor of 2. The resonance parameters of Horen *et al.* [9] are in good agreement with our data.

B. Capture cross-section data

In Fig. 4 the yield (C_w/φ_n) is compared with the background component (B_w/φ_n) and the contribution due to the neutron

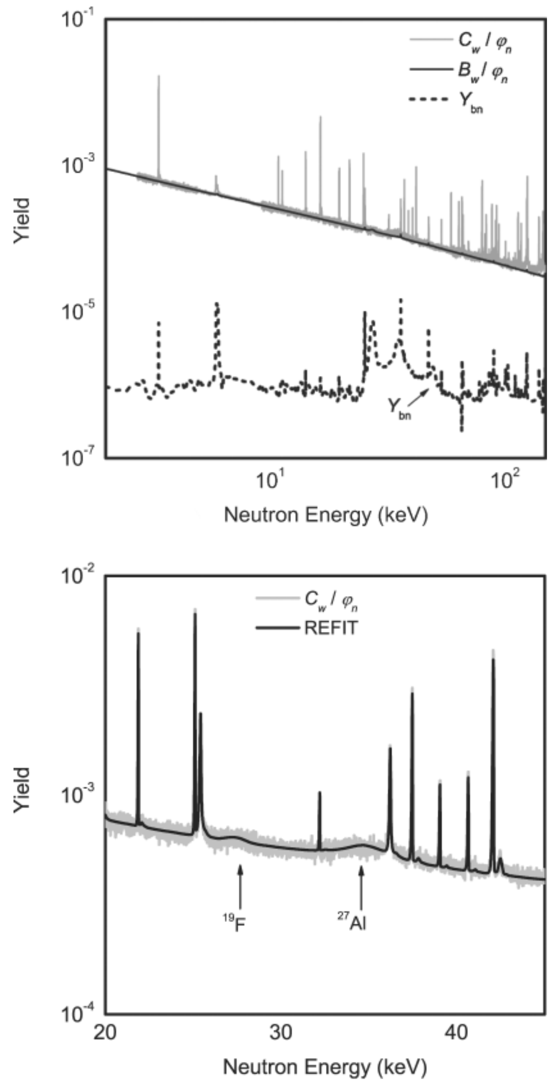

FIG. 4. The yield (C_w/φ_n) as function of neutron energy together with the background contribution (B_w/φ_n) and the contribution due to scattered neutrons ($Y_{\rm bn}$). The bottom figure shows the result of an analysis around the 27- and 35-keV resonances of ^{19}F and ^{27}Al, respectively.

sensitivity of the detection system $Y_{\rm bn}$. In the REFIT code the total background Y_b can be described by a sum of two components:

$$Y_b(T_n) = \frac{b_0 + b_1 T_n^{b_2} + \sum_{i=3,5} b_i e^{-b_{i+1}T_n}}{\varphi_n(T_n)} + Y_{\rm bn}. \quad (8)$$

The first component, which includes an analytical expression for the contribution B_w in Eq. (2), is the main source of background and depends on the measurement conditions. Its contribution can be adjusted through the parameters b_i, which can be defined as free-fitting parameters. The efficiency $\epsilon_{\rm nw}$ in Eq. (5) was deduced from Monte Carlo simulations with the code MCNP, version 4C3 [27], applying the weighting function that was used for the calculation of the experimental yield. Figure 4 shows the impact of the neutron sensitivity on the structures observed in the experimental yield. The structures around neutron energies 27 and 35 keV are due to resonances in ^{19}F and ^{27}Al, respectively. The good agreement between the calculated and experimental yields in this region demonstrates that the magnitude of the neutron sensitivity correction that is applied in this work is well described. For resonances below 200 keV, the largest influence due to the neutron sensitivity was observed for the 160.2-keV resonance and resulted in a 3% contribution to the total resonance area. Not all analysis codes include a direct correction for the neutron sensitivity in the description of the experimental yield as in Eq. (4). In such a case (see, e.g., Ref. [28]) a correction is applied to the observed radiation width, which is deduced from a resonance analysis without accounting for the neutron sensitivity. When the contribution due to neutron sensitivity is not included in the resonance shape analysis, the radiation width of the 160.2-keV resonance is underestimated by almost 10% [13].

In Fig. 5 the capture kernels $K_\gamma = g\Gamma_n\Gamma_\gamma/(\Gamma_n + \Gamma_\gamma)$ for the most important resonances below 200 keV are compared with the data of Mizumoto *et al.* [4] and Allen *et al.* [3]. The results of Ref. [4] have been corrected for the factor quoted by Macklin and Winters [29]. When the doublet at 47.5 keV is neglected our data are on average about 10% lower than those of Mizumoto *et al.* [4], with fluctuations around 7%. A comparison with the data of Allen *et al.* [3] shows larger discrepancies. The capture kernel for the resonances at 3.3 and 14.2 keV obtained in this work deviate significantly from the data of Allen *et al.* [3] and are in much better agreement with those of Ref. [4]. Mizumoto *et al.* [4] pointed already out that the data in Ref. [3] were taken with a relatively thick sample and suffer from systematic effects due to the correction for self-shielding and multiple scattering. Borella *et al.* [26] compared the capture area obtained with the detector placed at 125° and 90° with respect to the incoming neutron beam with the results of Mizumoto *et al.* [4] and concluded that the data of Refs. [4] and [3] suffer from a systematic uncertainty due to the anisotropy effects for resonances with a spin $J > 1/2$ and $\ell > 0$. Additional systematic differences can be explained by the fact that in Refs. [4] and [3] the applied weighting functions did not account for the γ-ray transport in the sample.

Figure 5 shows that even larger discrepancies are noticed when comparing our data with the data of Musgrove and Macklin [5]. The ratio of their capture area relative to the one obtained in this work increases with energy. Due to the limited resolution for the measurements in Ref. [5] not all resonances were separated and the observed capture area was overestimated. Figure 5 also suggests a different behavior for two groups of resonances. This might be related to the fact that part of the results in Ref. [5] were obtained from area analysis and another part from resonance shape analysis. It is thought that the discrepancies with the data of Allen *et al.* [3], Mizumoto *et al.* [4], and Musgrove and Macklin [5] are due to various reasons such as the difference in resolution of the time-of-flight spectrometer, the correction for multiple scattering and self-shielding correction, the use of weighting functions not accounting for the γ-ray transport in the sample, angular correlation effects, and the neutron sensitivity of the detection systems and its correction.

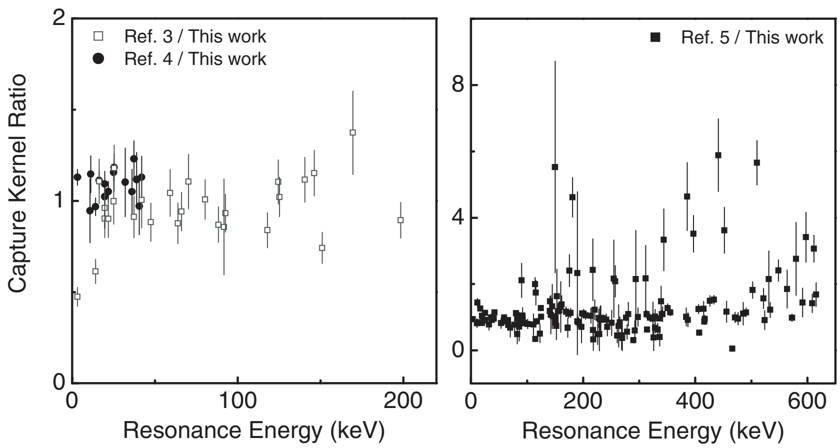

FIG. 5. The ratio of the capture kernel obtained by Allen *et al.* [3] (left), Mizumoto *et al.* [4] (left), and Musgrove and Macklin [5] (right) relative to the area obtained in this work as a function of the resonance energy.

C. Primary γ-ray intensities

Partial capture cross sections were already reported by Biggerstaff *et al.* [30] and Mizumoto *et al.* [4]. From measurements with a Ge detector, Mizumoto *et al.* [4] concluded that the γ-ray spectra of nine resonances between 3.36 and 42.07 keV are composed of fewer than five discrete γ-ray cascades. To verify these results, the C_6D_6 spectra of some resonances were unfolded using response functions corresponding to given γ-ray cascades.

In total the spectra for 22 resonances below 70 keV were obtained. The contributions of the cascade with a primary transition to the ground state and to the first and second excited state, with $E_\gamma - E_0 = 6738$, 6169, and 5841 keV, respectively, were determined by a linear least-squares fit to the spectra using the expression:

$$\chi^2 = \sum_{E_d} \left[\frac{C(E_d) - \sum_{k=1}^{3} A_k Y_k(E_d)}{\sigma(E_d)} \right]^2, \tag{9}$$

where $C(E_d)$ is the experimental spectrum of the energy E_d, $\sigma^2(E_d)$ is the variance due to counting statistics, and E_0 is the resonance energy. The normalized response corresponding to the γ-ray cascades with primary transitions $E_\gamma - E_0 =$ 6738, 6169, and 5841 keV are expressed as Y_k with $k = 1$, 2, and 3, respectively, and their intensities are given by A_k. The responses Y_k were determined by Monte Carlo simulations using the γ-ray transition data of Ref. [31]. The χ^2 is minimized, including only events with an energy deposition above 3500 keV, a region that is dominated by the contributions of the three aforementioned transitions. The complete C_6D_6 spectrum could be described by a weighted sum of these three transitions for only the 11.29-, 16.42-, 19.74-, and 65.99-keV resonances. For the 16.42-keV resonance this is illustrated in Fig. 6. For the other resonances, the C_6D_6 spectrum cannot be reproduced by contributions of these cascades alone. For example, for the 3.36-keV resonance about 40% of the response results from cascades with a primary energy smaller than 5.8 MeV. The structure of the C_6D_6 response functions does not allow differentiation between the contributions of other cascades, such as the transitions to the levels at 2623 and 3299 keV, respectively. The result of the fitting procedure for the 3.36 keV is shown in Fig. 6.

The relative intensities I_γ in Table II were normalized to the total content of the C_6D_6 response. Table II also shows the total contribution of other cascades, which cannot be neglected. Our data confirm the results of Ref. [4] only for the 11.29- and 16.42-keV resonances. The γ-ray resolving power of the Ge(Li) detector used by Mizumoto *et al.* [4] is far superior compared to the resolving power of the C_6D_6 detectors used in this work. However, due to both the bad time resolution and the high neutron sensitivity of the Ge(Li) detector, the γ-ray

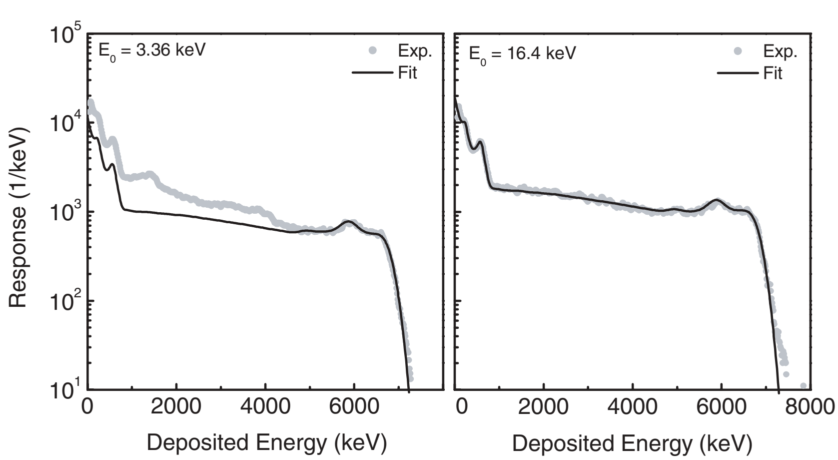

FIG. 6. The measured and fitted C_6D_6 pulse height spectra for the ^{206}Pb resonances at 3.36 keV (left) and 16.4 keV (right). The latter ones are the sum of the contributions Y_k = 1, 2, 3.

TABLE II. Relative emission probabilities I_γ of primary γ rays from the ^{206}Pb(n, γ) reaction for resonances below 70 keV.

E_0 (keV)	I_{6738}	I_{6169}	I_{5841}	I_{other}
3.358	0.40 ± 0.02	0.05 ± 0.02	0.15 ± 0.02	0.40
10.864		0.85 ± 0.04		0.15
11.296	1.00 ± 0.03			0.00
14.218	0.12 ± 0.02		0.58 ± 0.04	0.30
16.426	0.75 ± 0.04		0.25 ± 0.03	0.00
19.741		0.25 ± 0.03	0.70 ± 0.05	0.05
19.806		0.65 ± 0.04		0.35
21.879	0.08 ± 0.02	0.47 ± 0.03		0.45
25.109	0.52 ± 0.02	0.08 ± 0.02		0.40
25.424	0.10 ± 0.02	0.65 ± 0.03		0.25
32.199		0.05 ± 0.02	0.15 ± 0.05	0.80
36.211	0.08 ± 0.01	0.70 ± 0.04	0.07 ± 0.02	0.15
37.464	0.25 ± 0.02	0.50 ± 0.03		0.25
39.037	0.03 ± 0.01	0.27 ± 0.04	0.48 ± 0.04	0.22
40.647		0.22 ± 0.03	0.60 ± 0.03	0.18
42.071		0.15 ± 0.02	0.60 ± 0.03	0.25
47.502	0.08 ± 0.02	0.55 ± 0.04	0.15 ± 0.03	0.22
53.905	0.10 ± 0.02	0.30 ± 0.03	0.35 ± 0.03	0.25
59.221		0.08 ± 0.02	0.54 ± 0.02	0.38
63.952		0.45 ± 0.03	0.10 ± 0.03	0.45
65.996	1.00 ± 0.02			<0.04
66.584	0.03 ± 0.01	0.50 ± 0.05	0.37 ± 0.05	0.10

spectra of Ref. [4] can be contaminated by the contribution of neighboring resonances and neutrons scattered by the sample. For example, Mizumoto *et al.* [4] were not able to resolve the resonance doublets around 19.8 and 25.2 keV.

V. DISCUSSION

A. Resonance parameters

The final resonance parameters deduced from a simultaneous analysis of the capture and transmission data below 620 keV are listed in Table III and in the EXFOR data file [32]. In the analysis resonances above 620 keV were included taking the parameters of ENDF/B-VI.8. The channel radius was taken identical to the effective scattering radius $R' =$ 9.54 fm and one negative resonance was included to adjust the thermal scattering cross section at 0.0253 eV to 10.68 b and the capture cross section to 27 mb. The former is deduced from the coherent scattering length 9.22 ± 0.07 fm obtained by Ioffe *et al.* [33] and 9.23 ± 0.05 fm by Koester and Knopf [34]. The latter results from a combination of the value 26.6 ± 1.2 mb quoted by Blackmon *et al.* [35] and the value 27.3 ± 0.8 mb recently obtained at the Budapest Neutron Center [14]. Because our transmission data are limited to an energy up to 80 keV, only the neutron widths for resonances below 80 keV were adjusted. The neutron widths for resonances above 80 keV were kept fixed at the values listed in the ENDF/B-VI.8 library, which are mainly based on the data of Horen *et al.* [9]. Because the REFIT code is based on a least-squares adjustment, all parameters quoted with an uncertainty result directly from our measurement data. Therefore, they are independent from any prior information on these values.

In the region up to 620 keV, 304 resonances were observed and analyzed compared to only 234 resonances by Horen *et al.* [9], 156 by Musgrove and Macklin [5], and 221 listed in the ENDF/B-VI.8 library. No evidence was found for the resonances at 269.77, 283.13, and 589.22 keV, which were previously reported by Horen *et al.* [9]. For the resonances not observed by Horen *et al.* [9,10] only the resonance energy and the capture area resulting from our capture measurements are given. For 24 resonances the capture area is not reported because the uncertainty due to counting statistics was too high. For the resonances at 10.9, 11.3, and 32.2, only the neutron width and the capture area are given. For these resonances $\Gamma_n \ll \Gamma_\gamma$ and the capture data do not provide additional information with respect to the transmission data. For these resonances the total observed width is dominated by the resolution broadening and hence the radiation width cannot be deduced from a resonance shape analysis of the capture data.

The given uncertainties on the resonance parameters result only from counting statistics and spectra manipulations such as dead time and background corrections. They do not include the common uncertainty component on the capture data due to the normalization, the weighting function and the shape of the neutron flux. These effects together result in a 2% total correlated uncertainty for the capture data. The correlated uncertainty component of the total cross section data is 0.5%, mainly due to the normalization.

For the 3.35-keV p-wave resonance the simultaneous analysis of the capture and transmission data results in a

TABLE III. Resonance parameters for ^{206}Pb+n. The quoted uncertainties are due to counting statistics and do not include correlated components due to the flight path length and normalization. For the resonances marked with an asterisk only the capture kernel was deduced.

E_0 (eV)	J	ℓ	$g\Gamma_n$ (eV)	$g\Gamma_\gamma$ (eV)	$g\Gamma_n\Gamma_\gamma/\Gamma$ (eV)
−10000.0	0.5	0	76.5	0.53	
3357.6	1.5	1	0.570 ± 0.004	0.146 ± 0.001	0.116 ± 0.001
10863.7	1.5	1	0.065 ± 0.006		0.055 ± 0.007
11295.7	0.5	1	0.042 ± 0.001		0.041 ± 0.001
14218.0	0.5	1	1.559 ± 0.026	0.135 ± 0.002	0.124 ± 0.001
16426.4	0.5	0	0.788 ± 0.005		0.597 ± 0.006
19741.1	1.5	1	2.584 ± 0.057	0.140 ± 0.002	0.133 ± 0.002
19805.5	1.5	1	0.161 ± 0.003		0.130 ± 0.002
21879.1	1.5	1	1.749 ± 0.056	0.271 ± 0.004	0.235 ± 0.003
25108.8	1.5	1	1.240 ± 0.061	0.568 ± 0.016	0.390 ± 0.010
25424.2	0.5	1	48.860 ± 0.102	0.291 ± 0.002	0.289 ± 0.002
32199.1	1.5	1	0.053 ± 0.002		0.049 ± 0.002
36210.9	0.5	1	35.710 ± 0.178	0.280 ± 0.003	0.278 ± 0.003
37464.4	1.5	1	1.779 ± 0.133	0.460 ± 0.011	0.365 ± 0.009
39036.8	1.5	1	0.121 ± 0.004		0.103 ± 0.003
40647.3	0.5	1	0.884 ± 0.125	0.158 ± 0.005	0.134 ± 0.005
42071.1	1.5	1	1.966 ± 0.163	1.171 ± 0.082	0.734 ± 0.039
47501.8	0.5	1	83.160 ± 0.286	0.111 ± 0.002	0.111 ± 0.002
47544.0*					0.102 ± 0.007
53905.3	1.5	1	13.132 ± 0.327	0.159 ± 0.003	0.158 ± 0.003
59220.7*					0.644 ± 0.015
63951.6	2.5	2	3.330 ± 0.328	0.680 ± 0.017	0.565 ± 0.015
65996.0	0.5	0	82.210 ± 0.414	1.398 ± 0.018	1.375 ± 0.017
66584.3	1.5	1	19.062 ± 0.475	0.363 ± 0.006	0.356 ± 0.006
67493.2*					0.029 ± 0.003
70283.4	0.5	1	10.780 ± 0.386	0.086 ± 0.003	0.085 ± 0.003
78009.2	1.5	1	6.656 ± 0.523	0.058 ± 0.005	0.057 ± 0.005
80173.1*					0.167 ± 0.116
80366.7	1.5	2	14.000	2.526 ± 0.022	2.141 ± 0.016
80887.8*					0.050
82714.0*					0.201 ± 0.117
82913.2	1.5	2	16.000	0.233 ± 0.007	0.230 ± 0.007
83613.5*					0.553 ± 0.285
86122.4	0.5	1	16.000	0.070 ± 0.006	0.070 ± 0.005
88444.2	2.5	2	24.000	1.214 ± 0.014	1.156 ± 0.013
90124.5	1.5	1	150.000	0.102 ± 0.008	0.102 ± 0.008
91733.1*					0.553 ± 0.114
92612.0	0.5	0	32.000	1.503 ± 0.017	1.436 ± 0.016
94742.9	1.5	2	14.000	0.578 ± 0.008	0.555 ± 0.008
99721.0*					0.044
101209.2	2.5	2	24.000	0.280 ± 0.004	0.277 ± 0.003
104252.3	0.5	1	65.000	0.151 ± 0.002	0.150 ± 0.002
105149.7*					0.047
109216.6*					0.072 ± 0.008
111139.3	1.5	1	60.000	0.155 ± 0.002	0.155 ± 0.002
113028.3*					0.053
114359.1	1.5	1	5.000	1.148 ± 0.123	0.934 ± 0.081
114525.1	2.5	2	16.800	1.211 ± 0.021	1.130 ± 0.018
115728.0	1.5	1	11.400	0.169 ± 0.009	0.167 ± 0.009
117978.3	2.5	2	15.300	1.090 ± 0.017	1.017 ± 0.015
123119.4	0.5	1	35.000	0.129 ± 0.010	0.129 ± 0.010
123684.7*					0.242 ± 0.018
124596.1	1.5	2	300.000	3.678 ± 0.040	3.383 ± 0.033
124774.0*					0.091
125235.6	1.5	2	42.000	8.726 ± 0.061	7.225 ± 0.042

TABLE III. *(Continued.)*

E_0 (eV)	J	ℓ	$g\Gamma_n$ (eV)	$g\Gamma_\gamma$ (eV)	$g\Gamma_n\Gamma_\gamma/\Gamma$ (eV)
126038.3*					0.390
127884.5*					0.073 ± 0.015
140060.9*					0.155 ± 0.072
140540.9	1.5	2	206.000	3.038 ± 0.032	2.994 ± 0.032
140910.0	1.5	1	56.000	0.132 ± 0.003	0.132 ± 0.003
141947.4*					0.107
142312.8	0.5	1	12.000	0.142 ± 0.013	0.140 ± 0.012
144709.4	1.5	2	6.200	0.284 ± 0.017	0.272 ± 0.015
146272.3	0.5	0	176.000	5.128 ± 0.044	4.983 ± 0.042
149896.2	1.5	1	1194.200	0.095 ± 0.025	0.095 ± 0.025
150622.0	0.5	1	4.400	0.263 ± 0.016	0.248 ± 0.014
151052.3	2.5	2	57.000	1.579 ± 0.025	1.537 ± 0.023
152097.9	2.5	2	1.500	0.254 ± 0.016	0.217 ± 0.012
153199.8	0.5	1	10.000	0.229 ± 0.016	0.224 ± 0.016
153458.2*					0.168 ± 0.014
155272.4*					0.318 ± 0.028
159973.3	1.5	1	136.000	0.107 ± 0.013	0.107 ± 0.013
161569.0	2.5	2	1.800	0.325 ± 0.017	0.275 ± 0.012
169431.7*					0.815 ± 0.054
172712.1	1.5	1	146.000	0.280 ± 0.016	0.280 ± 0.016
173705.4	1.5	2	94.000	0.705 ± 0.021	0.700 ± 0.020
175597.6	1.5	1	26.000	0.262 ± 0.033	0.260 ± 0.032
175920.0*					0.315
177551.2*					0.688 ± 0.023
181121.7	1.5	1	54.000	0.233 ± 0.016	0.232 ± 0.015
183285.6*					0.186
185275.4*					0.159
189457.2	1.5	1	400.000	0.470 ± 0.023	0.470 ± 0.023
189793.5*					0.043 ± 0.034
191242.9	0.5	1	97.000	0.671 ± 0.024	0.667 ± 0.024
193416.8*					0.114 ± 0.016
196879.3	0.5	1	64.000	0.128 ± 0.019	0.128 ± 0.019
196904.7*					0.127 ± 0.021
198445.0	1.5	2	264.000	6.106 ± 0.059	5.965 ± 0.056
199677.4*					0.249
200638.6	1.5	1	24.000	1.708 ± 0.035	1.595 ± 0.030
202965.2*					0.140
204152.5	1.5	2	470.000	1.288 ± 0.030	1.284 ± 0.030
209508.7	0.5	0	2173.000	1.230 ± 0.021	1.229 ± 0.021
209946.1*					0.847
211794.0*					0.026
213789.8	1.5	2	44.000	0.910 ± 0.026	0.892 ± 0.025
217197.2*					0.212 ± 0.039
217215.5	1.5	1	20.000	0.171 ± 0.020	0.169 ± 0.020
217554.2	0.5	1	22.000	0.124 ± 0.020	0.123 ± 0.020
218053.5	0.5	1	6.200	0.092 ± 0.018	0.091 ± 0.017
220804.0	0.5	0	1407.000	0.698 ± 0.048	0.698 ± 0.048
223253.6*					0.062
226036.6*					0.330 ± 0.050
227951.3*					0.720 ± 0.037
229011.2	1.5	1	70.000	0.083 ± 0.020	0.083 ± 0.020
230248.4	2.5	2	120.000	0.520 ± 0.025	0.518 ± 0.024
231212.4*					0.471 ± 0.040
233143.6*					0.249 ± 0.026
235422.0	1.5	2	214.000	2.740 ± 0.048	2.706 ± 0.046
239627.4*					0.135 ± 0.021
240746.3*					0.378 ± 0.033

TABLE III. *(Continued.)*

E_0 (eV)	J	ℓ	$g\Gamma_n$ (eV)	$g\Gamma_\gamma$ (eV)	$g\Gamma_n\Gamma_\gamma/\Gamma$ (eV)
241445.0	1.5	1	78.000	1.485 ± 0.037	1.458 ± 0.035
243208.2∗					0.763 ± 0.035
244987.1∗					0.225 ± 0.023
250818.3	2.5	2	156.000	0.528 ± 0.028	0.526 ± 0.028
253716.0∗					0.141
254703.3∗					0.139 ± 0.029
257429.8	0.5	0	1427.000	0.889 ± 0.059	0.889 ± 0.059
260674.5∗					0.982 ± 0.405
263092.5	1.5	1	108.000	0.238 ± 0.028	0.237 ± 0.028
265563.3	1.5	2	80.000	1.703 ± 0.044	1.667 ± 0.042
268387.3	1.5	1	212.000	0.123 ± 0.028	0.123 ± 0.028
269637.9	1.5	2	106.000	0.109 ± 0.027	0.109 ± 0.027
271508.7∗					0.117 ± 0.022
273603.1∗					0.155
274391.3	0.5	1	32.000	0.554 ± 0.033	0.545 ± 0.032
276567.1	1.5	2	224.000	6.540 ± 0.083	6.355 ± 0.079
278374.4	2.5	2	299.900	0.902 ± 0.041	0.899 ± 0.041
280579.2	0.5	1	171.000	1.139 ± 0.046	1.132 ± 0.046
289501.9∗					1.320 ± 0.052
292044.6∗					0.337 ± 0.036
293878.3	1.5	1	220.000	0.112 ± 0.032	0.112 ± 0.032
295193.5∗					0.200
297684.5	0.5	0	113.000	1.282 ± 0.046	1.268 ± 0.045
298593.7∗					0.216
299689.5	0.5	1	62.000	1.028 ± 0.047	1.011 ± 0.045
299736.1∗					0.184
303828.2∗					1.909
306399.9	0.5	1	73.000	0.154 ± 0.031	0.154 ± 0.031
311404.9	2.5	2	6.600	0.168 ± 0.032	0.164 ± 0.031
313281.8	1.5	2	44.000	2.502 ± 0.065	2.367 ± 0.058
314263.4	2.5	2	536.700	2.525 ± 0.063	2.513 ± 0.062
317082.6∗					0.150
319233.9	1.5	2	328.000	1.791 ± 0.056	1.782 ± 0.056
320657.0∗					0.272
324391.9	1.5	1	109.900	0.505 ± 0.040	0.503 ± 0.039
325567.6	0.5	1	49.000	0.155 ± 0.036	0.155 ± 0.035
328189.8	1.5	1	88.100	1.092 ± 0.052	1.078 ± 0.051
328424.0	2.5	2	18.900	0.723 ± 0.053	0.697 ± 0.049
330412.1∗					0.202 ± 0.061
333062.8∗					1.597 ± 0.057
335563.8∗					0.271
336631.9	1.5	2	255.800	0.374 ± 0.043	0.374 ± 0.042
339209.1	2.5	2	47.900	0.720 ± 0.047	0.710 ± 0.045
340130.5	0.5	0	10870.000	4.670 ± 0.048	4.668 ± 0.048
340204.7	2.5	2	48.000	0.291 ± 0.044	0.289 ± 0.043
341779.5	1.5	2	347.800	1.354 ± 0.060	1.349 ± 0.060
343969.5	1.5	2	169.900	0.273 ± 0.047	0.273 ± 0.047
345286.3	2.5	2	227.900	1.142 ± 0.053	1.136 ± 0.052
346588.0∗					0.241 ± 0.077
348017.8∗					0.183 ± 0.045
350810.5	1.5	2	423.800	4.010 ± 0.087	3.972 ± 0.085
355634.2	0.5	0	5302.000	5.870 ± 0.170	5.865 ± 0.170
356688.9	2.5	2	92.900	1.707 ± 0.069	1.676 ± 0.067
357730.4	1.5	2	909.400	1.900 ± 0.081	1.896 ± 0.081
361692.4	0.5	1	80.000	0.518 ± 0.056	0.515 ± 0.055
362440.7	1.5	2	195.900	1.292 ± 0.063	1.283 ± 0.062
362956.8	1.5	1	72.000	0.533 ± 0.056	0.530 ± 0.055

TABLE III. *(Continued.)*

E_0 (eV)	J	ℓ	$g\Gamma_n$ (eV)	$g\Gamma_\gamma$ (eV)	$g\Gamma_n\Gamma_\gamma/\Gamma$ (eV)
363764.0	1.5	1	67.900	0.283 ± 0.045	0.282 ± 0.045
368380.1*					0.450 ± 0.128
370277.4	1.5	2	90.000	0.959 ± 0.059	0.949 ± 0.058
371089.3	0.5	1	40.000	0.151 ± 0.047	0.151 ± 0.047
374553.0*					0.498 ± 0.062
376643.9	2.5	2	572.700	0.522 ± 0.058	0.522 ± 0.058
378157.9	0.5	0	4419.000	2.870 ± 0.047	2.869 ± 0.047
378196.2*					0.478
383981.9	2.5	2	843.000	1.295 ± 0.069	1.293 ± 0.069
385451.0	0.5	1	157.100	0.466 ± 0.056	0.464 ± 0.056
386782.4	1.5	2	158.000	1.996 ± 0.082	1.971 ± 0.080
389555.5	0.5	0	4365.000	2.443 ± 0.135	2.442 ± 0.135
393351.7*					0.657 ± 0.115
396766.0*					1.933 ± 0.108
400101.6	2.5	2	414.900	2.036 ± 0.076	2.026 ± 0.075
403848.7	0.5	1	173.000	0.565 ± 0.061	0.564 ± 0.061
405751.7	2.5	2	306.000	5.619 ± 0.111	5.515 ± 0.107
407142.6	1.5	2	141.900	5.448 ± 0.114	5.245 ± 0.106
408039.2	0.5	1	44.000	0.548 ± 0.065	0.542 ± 0.064
412273.7	0.5	1	126.000	0.456 ± 0.059	0.454 ± 0.058
414769.4	1.5	2	99.900	1.832 ± 0.082	1.799 ± 0.079
416248.9	2.5	2	920.700	6.150 ± 0.123	6.110 ± 0.121
417032.9	0.5	0	6341.000	5.125 ± 0.229	5.120 ± 0.229
420076.2	2.5	2	102.000	0.950 ± 0.072	0.942 ± 0.071
421560.7*					0.244 ± 0.171
425900.0	1.5	2	1043.000	5.170 ± 0.132	5.145 ± 0.131
426498.4	2.5	2	50.900	1.093 ± 0.092	1.070 ± 0.088
427947.2	0.5	1	127.800	0.435 ± 0.065	0.433 ± 0.065
429864.4	0.5	0	129.000	0.772 ± 0.065	0.767 ± 0.064
433258.7	2.5	2	140.900	8.022 ± 0.147	7.590 ± 0.132
433849.5	1.5	2	116.100	2.104 ± 0.120	2.067 ± 0.116
435429.9*					1.640 ± 0.311
438150.6*					0.357 ± 0.227
439366.3	0.5	1	36.000	0.516 ± 0.065	0.509 ± 0.063
441141.9	1.5	2	218.000	0.936 ± 0.082	0.933 ± 0.082
442013.2	2.5	2	42.000	3.252 ± 0.105	3.019 ± 0.091
444269.1	2.5	2	32.900	0.397 ± 0.058	0.392 ± 0.057
445441.3	1.5	1	353.400	0.232 ± 0.063	0.232 ± 0.063
446326.5	2.5	2	35.900	0.616 ± 0.074	0.606 ± 0.072
448619.2*					0.197 ± 0.156
452003.3	2.5	2	108.100	1.541 ± 0.094	1.519 ± 0.091
452194.9	1.5	2	87.900	0.390 ± 0.129	0.388 ± 0.128
452602.2	2.5	2	16.500	1.996 ± 0.122	1.781 ± 0.097
453413.4	0.5	1	59.000	0.394 ± 0.070	0.391 ± 0.069
454507.7	1.5	1	50.000	0.224 ± 0.022	0.223 ± 0.022
455470.8	0.5	0	42.000	1.980 ± 0.091	1.891 ± 0.083
458225.4	0.5	1	43.000	0.305 ± 0.059	0.302 ± 0.059
459949.8	2.5	2	48.000	0.341 ± 0.059	0.338 ± 0.058
461730.6	1.5	1	30.000		0.100 ± 0.060
462155.3	2.5	2	27.000	0.486 ± 0.054	0.478 ± 0.052
466008.9*					171.500 ± 3.788
467507.4	1.5	1	180.000	12.316 ± 1.848	11.525 ± 1.619
470955.1	1.5	2	321.800	5.848 ± 0.130	5.745 ± 0.125
471787.1	1.5	1	124.000		0.044
472764.7	2.5	3	123.000	1.157 ± 0.074	1.147 ± 0.072
474874.0*					1.425
476608.1	0.5	0	373.700	2.751 ± 0.107	2.731 ± 0.105

TABLE III. *(Continued.)*

E_0 (eV)	J	ℓ	$g\Gamma_n$ (eV)	$g\Gamma_\gamma$ (eV)	$g\Gamma_n\Gamma_\gamma/\Gamma$ (eV)
478304.6*					0.775 ± 0.164
481346.7	0.5	0	9061.000	1.781 ± 0.518	1.781 ± 0.518
481720.0*					0.517
483732.4	0.5	1	101.900	0.835 ± 0.077	0.828 ± 0.076
485487.6	2.5	2	98.900	2.699 ± 0.099	2.627 ± 0.094
488593.4*					0.355 ± 0.152
489497.6	2.5	2	42.100		0.868 ± 0.629
490504.2	1.5	2	147.900	6.654 ± 0.184	6.370 ± 0.168
493561.5	2.5	2	86.900	1.053 ± 0.077	1.040 ± 0.076
495962.0	1.5	2	38.000	1.539 ± 0.092	1.479 ± 0.085
498024.5	0.5	1	289.400	1.151 ± 0.084	1.147 ± 0.083
501377.6	1.5	1	52.100	1.387 ± 0.121	1.351 ± 0.115
501990.9	2.5	2	456.000	3.717 ± 0.136	3.687 ± 0.134
503105.1	1.5	2	64.100	1.397 ± 0.100	1.368 ± 0.095
504224.1*					0.716 ± 0.118
506718.5*					1.344 ± 0.177
510006.5	2.5	2	267.000	1.834 ± 0.126	1.821 ± 0.124
510619.1	1.5	2	171.900	2.784 ± 0.149	2.740 ± 0.144
511396.1	2.5	2	47.900		2.607 ± 1.429
511396.8	1.5	1	246.000		0.414
511780.5	0.5	0	160.000	2.626 ± 0.152	2.584 ± 0.147
513593.4	0.5	1	4.200	0.512 ± 0.094	0.456 ± 0.075
515548.2	2.5	2	20.400	0.586 ± 0.081	0.570 ± 0.076
517677.1	0.5	1	110.200	1.069 ± 0.091	1.059 ± 0.089
519140.0	2.5	2	65.900	0.658 ± 0.069	0.652 ± 0.068
520483.1	2.5	2	562.800	0.521 ± 0.094	0.520 ± 0.094
521695.8	0.5	0	55.000	3.177 ± 0.132	3.003 ± 0.118
523729.4	1.5	2	321.800	3.212 ± 0.121	3.181 ± 0.118
529837.5	2.5	2	53.800	0.307 ± 0.084	0.305 ± 0.083
530769.4	0.5	0	390.500	0.979 ± 0.106	0.977 ± 0.106
532054.4	2.5	2	101.800	1.475 ± 0.105	1.454 ± 0.102
533729.7	2.5	2	179.900	3.168 ± 0.120	3.113 ± 0.116
535613.8	0.5	1	62.100	0.558 ± 0.084	0.554 ± 0.083
537403.8	1.5	1	126.200	0.486 ± 0.083	0.484 ± 0.082
539133.6	2.5	2	92.400	0.769 ± 0.060	0.763 ± 0.059
541301.4	1.5	2	1032.600	1.396 ± 0.110	1.395 ± 0.110
544008.3*					1.401 ± 0.180
546997.4	2.5	2	22.000	0.608 ± 0.054	0.592 ± 0.051
548171.3	0.5	0	3096.000	3.121 ± 0.196	3.118 ± 0.195
549940.4	1.5	1	63.900	0.305 ± 0.091	0.304 ± 0.090
551677.9	2.5	2	155.800	1.622 ± 0.102	1.606 ± 0.100
555776.3	1.5	2	26.100	0.612 ± 0.090	0.599 ± 0.086
557642.0	0.5	1	120.100	1.646 ± 0.103	1.624 ± 0.100
559460.8*					0.540 ± 0.108
561436.7*					0.534 ± 0.103
563623.7	1.5	1	506.400	2.118 ± 0.119	2.110 ± 0.118
564809.3	0.5	1	14.000	1.113 ± 0.124	1.031 ± 0.106
566293.6	2.5	2	30.000	2.887 ± 0.141	2.634 ± 0.117
568559.4*					0.780 ± 0.248
570745.7	1.5	2	112.000	0.852 ± 0.162	0.846 ± 0.160
572598.5	2.5	2	2382.000	13.938 ± 0.269	13.855 ± 0.266
577460.6	2.5	2	86.900	0.360 ± 0.108	0.358 ± 0.107
578533.4	1.5	2	71.900	0.588 ± 0.095	0.583 ± 0.094
579662.4	1.5	2	46.000	1.730 ± 0.135	1.668 ± 0.125
580626.7	2.5	2	623.100	1.662 ± 0.127	1.658 ± 0.127
582205.6	1.5	1	222.000	0.691 ± 0.103	0.689 ± 0.102
584282.9*					1.551 ± 0.142

TABLE III. *(Continued.)*

E_0 (eV)	J	ℓ	$g\Gamma_n$ (eV)	$g\Gamma_\gamma(eV)$	$g\Gamma_n\Gamma_\gamma/\Gamma$ (eV)
586909.0$*$					0.522 ± 0.207
591153.1	2.5	2	303.000	1.885 ± 0.122	1.874 ± 0.120
592703.6$*$					1.464 ± 0.209
595426.3	2.5	2	33.000	2.264 ± 0.140	2.119 ± 0.123
596042.8	0.5	1	84.000	0.715 ± 0.138	0.709 ± 0.136
597325.8	1.5	1	221.800	2.760 ± 0.148	2.727 ± 0.144
598130.5	2.5	2	86.900	2.030 ± 0.122	1.984 ± 0.116
600060.4	1.5	1	44.000	0.748 ± 0.109	0.736 ± 0.106
601679.8	2.5	2	10.500	0.716 ± 0.118	0.670 ± 0.103
603143.9	1.5	2	84.000	1.162 ± 0.114	1.147 ± 0.111
605642.5	0.5	1	75.000	1.205 ± 0.116	1.186 ± 0.112
608557.3	1.5	2	653.600	4.406 ± 0.178	4.377 ± 0.175
609877.4	0.5	0	3144.000	3.793 ± 0.165	3.788 ± 0.165
611420.1	1.5	2	399.200	4.722 ± 0.198	4.667 ± 0.193
612276.6	1.5	1	224.000		0.751
612286.8	1.5	2	420.200	3.982 ± 0.208	3.945 ± 0.204
614093.1	2.5	2	383.400	1.877 ± 0.157	1.869 ± 0.156
615481.4	2.5	2	1127.700	3.525 ± 0.204	3.514 ± 0.203
615938.1	1.5	2	249.800	2.626 ± 0.189	2.599 ± 0.185
616864.1	1.5	1	142.100	1.081 ± 0.154	1.073 ± 0.151
618408.7	2.5	2	18.900	1.590 ± 0.146	1.467 ± 0.124
618541.0	1.5	2	37.800	0.552 ± 0.132	0.544 ± 0.128
623000.0	2.5	2	1263.000	3.576	3.566
623900.0	0.5	1	232.000	0.340	0.339

resonance energy $E_0 = 3357.6 \pm 0.5$ eV. The uncertainty includes the uncertainty on the flight path length. This value is in good agreement with the energy $E_0 = 3357.4 \pm 0.4$ eV, which is considered as a neutron energy standard for time-of-flight measurements [36].

Figure 7 shows a comparison between the experimental capture yield with the calculated yield using the parameters deduced in this work and the ENDF/B-VI.8 resonance parameters, which are also used for the latest ENDF/B-VII.0 version [37]. Due to the lack of capture cross-section data above 200 keV, significant discrepancies in the radiation widths are observed. Similar discrepancies are observed when comparing the experimental yield with the yield obtained from other data libraries, such as JEFF 3.1 and JENDL 3.3. Our results have been partly included in the latest compilation of Mughabghab [38].

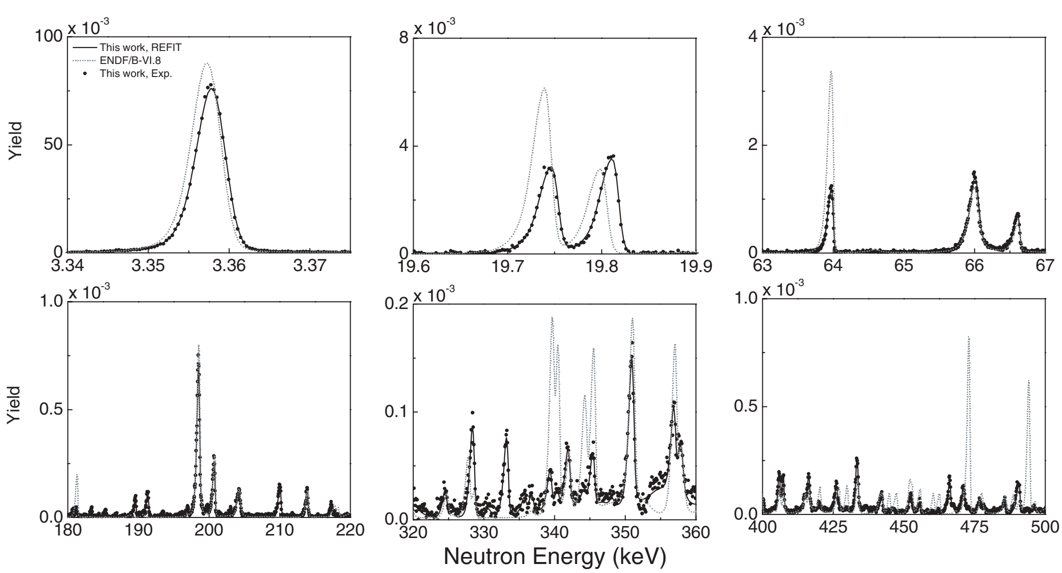

FIG. 7. The experimental yield, Y_{exp} as a function of neutron energy is compared with the yield obtained using the ENDF/B-VI.8 parameters and the parameters deduced in this work.

B. Average resonance parameters and strength functions

In this work only neutron widths up to a neutron energy of 80 keV were obtained. For the additional resonances, which were observed only in our capture data, not enough information is available to assign a spin and parity. Therefore, our data do not provide sufficient information to improve existing neutron strength functions and level densities. A detailed discussion on these parameters is given by Horen *et al.* [9,10].

Previous studies of the neutron-induced reactions ^{206,207,208}Pb+n demonstrated an intermediate structure in the energy region between 400 and 500 keV, which arises from a doorway state common to the ^{207,208,209}Pb compound systems [10]. The single resonance for ^{208}Pb+n at 506 keV appears to break up into a number of levels for ^{206}Pb+n and ^{207}Pb+n. Therefore, all three nuclei show a doorway state with the same escape width and spreading width that increases as one moves farther away from the doubly closed core nucleus ^{208}Pb. Measurements on ^{204}Pb show a constant reduced neutron strength function [39] with no evidence of a intermediate structure. Horen *et al.* [39] also noted the proportionality between the spreading width and the number of s-wave resonances. Divadeenam and Beres [40] showed that the s-wave doorway state for ^{206,207,208}Pb+n could be described in terms of a particle-vibration weak-coupling model involving the ^{208}Pb core (i.e., the $\nu g_{9/2}$ neutron single-particle state coupled to the 4^+ vibrational state, $4^+ \otimes \nu g_{9/2}$). They arrived at a good quantitative agreement between the theoretical estimate and the experimentally observed energy and escape width of the doorway state for ^{206,207,208}Pb+n. Using a quasiparticle-phonon nuclear model Soloviev *et al.* [41] obtained neutron strength functions for ^{206}Pb+n and ^{208}Pb+n that are in very good agreement with experimental data.

A doorway mechanism common to both the neutron and photon channel has been clearly observed for p-wave resonances of the ^{208}Pb compound system by Köhler *et al.* [42]. Baglan *et al.* [43] studied the photonuclear reaction ^{207}Pb(γ,n) and suggested that also for the ^{207}Pb compound system a correlation between the neutron and radiation width exists for s-wave resonances. Allen *et al.* [3,44] and Medsker and Jackson [45] performed ^{206}Pb(n,γ) and ^{207}Pb(γ,n) measurements, respectively, and found no evidence for the s-wave doorway state in the ground-state photon channel. Due to the doorway state in the neutron channel the reduced neutron widths for s-wave neutrons show an envelope structure as shown in Fig. 8. The radiation widths of primary transitions to the ground state for the 10 $1/2^+$ states observed in the ^{207}Pb(γ,n) measurements performed by Baglan *et al.* [43] show a similar structure. However, the s-wave radiation widths obtained from our capture data, which are given in Fig. 8, do not reveal such an envelope structure. A comparison of the widths obtained by Baglan *et al.* [43] with our data indicates that the widths obtained from the photonuclear measurements are overestimated. Allen *et al.* [44] and Medsker and Jackson [45] already suggested that due to the limited energy resolution a major part of the radiative strength attributed by Baglan *et al.* [43] to s-wave resonances in reality results from the background of much narrower resonances with $\ell \geqslant 1$. In addition, Baglan *et al.* [43] observed only 50% of the s-wave resonances below 600 keV.

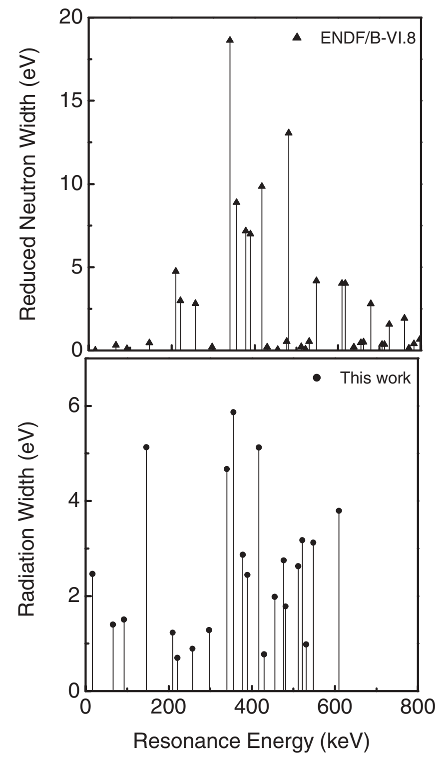

FIG. 8. The reduced neutron widths and the radiation widths for s-wave resonances in the ^{207}Pb compound system as a function of the resonance energy.

The unfolding of the C_6D_6 spectra (see Table II) shows that the γ-ray spectrum of the 66.0 keV s-wave resonance is completely dominated by an $E1$ transition to the ground state. Because the s-wave resonances contribute 30% of the thermal capture cross section and the γ-ray spectrum at thermal energy is dominated by the $E1$ transition to the ground state [14,35] it can be assumed that the radiation width for s-wave resonances results mainly from this $E1$ transition. Therefore, the radiation width for s-wave resonances of ^{206}Pb can be used to calculate the electrical dipole strength function using:

$$f_{\mathrm{XL}}(E_\gamma) = \frac{1}{D}\left\langle \frac{\Gamma_{\mathrm{XL}}(E_\gamma)}{E_\gamma^{2L+1}} \right\rangle \qquad (10)$$

with D the average level spacing. Using Eq. (10) a strength function $f_{E1} \leqslant (255 \pm 5) \times 10^{-9}$ MeV^{-3} for resonances up to 620 keV is obtained. This value is in good agreement with the value $f_{E1} = 228 \times 10^{-9}$ MeV^{-3} for a γ-ray transition from the capture state at the neutron threshold to the ground state obtained with the giant dipole parameters determined by Harvey *et al.* [46]. Our value deviates from the recommended value $f_{E1} = (109.8 \pm 7.8) \times 10^{-9}$ MeV^{-3}, which is based on systematics, and the value $f_{E1} = (366.1 \pm 26.1) \times 10^{-9}$ MeV^{-3} resulting from a compilation of experimental (photonuclear) data. These values were taken from RIPL2 [8]. From the relative transition probabilities in Table II together with the total radiation width of the p-wave resonances, the strength function for the magnetic dipole transition to the ground state, to the 570 keV $5/2^-$ first excited state and to the 897 keV

TABLE IV. The magnetic dipole strength function resulting from the p-wave resonances below 25 and 70 keV obtained in this work compared with the results from Mizumoto *et al.* [4]. The uncertainties on our data are in the order of 30%.

Reference	ΔE (keV)	$f_{M1,0}$ 10^{-9} MeV^{-3}	$f_{M1,570}$ 10^{-9} MeV^{-3}	$f_{M1,897}$ 10^{-9} MeV^{-3}
Ref. [4]	25	>60	>73	>25
This work	25	>33	>29	>27
This work	70	>17	>25	>20

$3/2^-$ second excited state can also be deduced. The resulting strength functions f_{M1} for the energy interval $\Delta E = 70$ keV, which are given in Table IV, are consistent with the value deduced from systematics $f_{M1} = 20 \times 10^{-9}$ MeV^{-3} [8]. Therefore, our data do not confirm the strong $M1$ enhancement suggested by Medsker and Jackson [45] and Mizumoto *et al.* [4]. To compare our data with those of Mizumoto *et al.* [4], the $M1$ strengths obtained for the resonances below 25 keV are also included in Table IV. Our data for resonances below 25 keV are a factor of 2 lower compared to the data of Mizumoto *et al.* [4]. Their strength functions were systematically overestimated because they supposed that the total radiation width resulted from four γ-ray cascades without accounting for other possible cascades. Due to the better time resolution of our capture measurements, the doublet around 25 keV, which has an important contribution to the strength function below 25 keV, has been resolved. In the data of Mizumoto *et al.* [4] these resonances were not resolved and the $M1$ γ-ray strength was overestimated by a factor of 2 because a part of the observed γ rays are $E2$ transitions. Indeed, for the p-wave resonances at 25.42, 36.21, and 47.50 keV a strong contribution of the primary γ-ray transition to the 569.7 keV $5/2^-$ level is observed. Because these resonances have a spin and parity $J^\pi = 1/2^-$, the most prominent primary γ rays for these resonances are $E2$ transitions. Although limited in number, the $E2$ transitions that were observed together with their radiation widths can be used to improve the systematic study of the average behavior of the electric quadrupole strength function f_{E2}. The partial radiation widths and the reduced transition probabilities $B(E2)\downarrow$ (downward) of these transitions (as defined in Ref. [47]) are listed in Table V. In the literature only a limited number of $E2$ primary transitions following neutron capture have been reported [48–50].

TABLE V. The total radiation width for the 25.4-, 36.2-, and 47.5-keV resonance together with the partial radiation width and reduced transition probability for the $E2$ transition to the first excited state. The quoted uncertainties result from counting statistics only.

E_0 (keV)	Γ_γ (eV)	$\Gamma_{\gamma,570}$ (eV)	$B(E2)\downarrow$ (e^2 fm^4)
25.4	0.291 ± 0.002	0.189 ± 0.008	25.7 ± 1.1
36.2	0.280 ± 0.003	0.196 ± 0.008	26.4 ± 1.1
47.5	0.111 ± 0.002	0.061 ± 0.005	8.1 ± 0.7

C. Stellar average capture cross sections

In stellar nuclear synthesis the relative velocities v between the neutrons and the nuclei have a Maxwell-Boltzman distribution at temperature T. Therefore, the neutron capture rates are proportional to the Maxwellian averaged capture (MAC) cross section:

$$\langle\sigma_\gamma\rangle_{kT} = \frac{2}{\sqrt{\pi}(kT)^2}\int_0^\infty \sigma_\gamma(E)E\exp\left(-\frac{E}{kT}\right)dE. \quad (11)$$

This quantity can be calculated numerically from the capture cross section. The energy range in which the cross section contributes to the integrand is, for ^{206}Pb, entirely in the resolved resonance region. For some resonances the radiation and neutron width could not be determined and only the capture area has been deduced. Therefore, the MAC cross sections obtained from the microscopic cross sections based on the resonance parameters will be underestimated. To calculate the Maxwellian-averaged capture cross sections the approximation proposed by Macklin and Gibbons [51] was applied:

$$\langle\sigma_\gamma\rangle_{kT} = \sigma_\gamma^0\sqrt{\frac{E_{th}}{kT}} + \frac{2}{\sqrt{\pi}}\frac{1}{(kT)^2} \times \sum_{i=1}^{N} A_{\gamma,i}E_{0,i}\exp\left(-\frac{E_{0,i}}{kT}\right), \quad (12)$$

where σ_γ^0 is the capture cross section at the thermal energy $E_{\mathrm{th}} = 0.0253$ eV, N the number of observed resonances, $E_{0,i}$ the resonance energy, and $A_{\gamma,i}$ the capture area, which is directly related to the capture kernel and the resonance energy. A detailed discussion about the limitations of this expression is given by Beer *et al.* [52]. The first term results in an upper limit for the combined effect of all distant s-wave resonances, including bound states, and the contribution due to direct s-wave capture. The second term represents the contribution of all observed resonances. The uncertainty on the MAC obtained by this approach is completely dominated by the 2% common uncertainty component. In Fig. 9 the resulting MAC cross sections using $\sigma_\gamma^0 = 27$ mb are given as a function of the

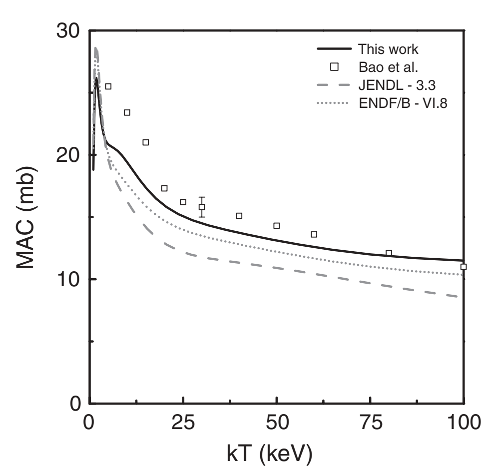

FIG. 9. The MAC cross section obtained in this work is compared with the one in Bao *et al.* [2] and the one deduced from the data in JENDL-3.3 and ENDF/B-VI.8.

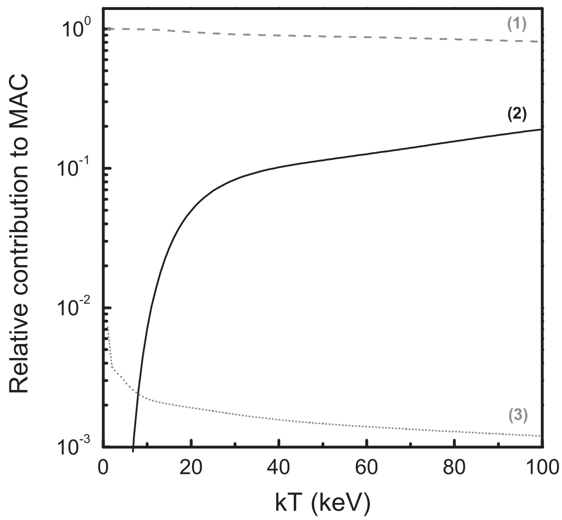

FIG. 10. The relative contribution to the MAC cross section of (1) the resonances listed in ENDF/B-VI.8, (2) the additional resonances for which the capture areas were deduced in this work and (3) the first term in Eq. (12).

energy kT. In Fig. 10 the relative contribution of the first term is shown together with the contribution of the resonances listed in ENDF/B-VI.8 using the capture area in Table III and the contribution of the 83 additional resonances that were observed in this work and not listed in ENDF/B-VI.8. The results in Fig. 10 show that the contribution due to the first term can be neglected.

However, the contribution at $kT = 30$ keV due the additional resonances is 8% and hence more than the required accuracy. For values of $kT > 80$ keV this contribution even amounts to 15%. Figure 9 compares our results with the data quoted in the most recent compilation of Bao *et al.* [2] and the MAC cross sections based on the microscopic data in JENDL 3.3 [53] and ENDF/B-VI.8. At an average temperature $kT = 30$ keV, the MAC cross section deduced in this work is about 8% smaller than the one compiled by Bao *et al.* [2] and 8 and 20% larger than the one in ENDF/B-VI.8 and JENDL-3.3, respectively. According to the sensitivity study performed by Ratzel *et al.* [1], one can conclude that the ^{206}Pb s-process abundance using the data of Bao *et al.* [2] is underestimated by 7%. The results in Fig. 10 indicate an overestimation of about 8% when the capture areas of the resonances that were observed in this work but not listed in ENDF/B-VI.8 are not included in the calculation.

VI. CONCLUSIONS

An accurate resonance parameter file for ^{206}Pb+n has been determined from high-resolution capture and transmission measurements at GELINA for resonances up to 620 keV. The use of an isotopically pure ^{206}Pb (99.82%) sample enabled an accurate determination of the effective scattering radius of 9.54 ± 0.02 fm for ^{206}Pb. From the transmission data the neutron width Γ_n for resonances up to 80 keV were deduced. The results from the actual transmission data agreed with the data of Horen *et al.* [9], which covered the energy region up to 900 keV. For the capture measurements special experimental conditions and data analysis procedures were implemented to reduce systematic bias effects as much as possible and to avoid correction factors requiring knowledge about the γ-ray emission cascade. Due to these precautions the correlated uncertainty component on the capture data was reduced to 2%. From the capture data, accurate total radiation widths were extracted. A comparison with data in the literature indicates that capture data previously reported suffer from systematic bias effects.

From the radiation width of the s-wave resonances observed below 620 keV a f_{E1} photon strength function was deduced. This strength function is consistent with the value deduced from GDR parameters obtained from photonuclear reactions. The f_{M1} strength function, derived from an unfolding of the C_6D_6 capture data, is consistent with the systematic behavior obtained from compiled data. It does not indicate any $M1$ enhancement as previously reported by other authors based on photonuclear data in the resonance region. Moreover, the presence of primary $E2$ transitions for ^{206}Pb was observed and their reduced radiation strength deduced. From an analysis of the reduced neutron width and radiation width, the existence of a doorway state in the photon channel, common to the doorway state in the neutron channel, could not be confirmed.

From the experimental observed capture areas up to 620 keV the MAC cross sections as function of temperature were derived with an accuracy better than the required 5%. The MACs obtained in this work are systematically lower than the values compiled by Bao *et al.* [2] and higher than the ones deduced from cross-section data in the evaluated data libraries. It is shown that the resonances, which were observed in this work and not reported in ENDF/B-VI.8, contribute for more than 8% to the MAC cross sections for energies above $kT = 30$ keV.

ACKNOWLEDGMENTS

The authors are grateful to W. Monderlaers and the GELINA operators for the dedicated and skillful running of the accelerator and to J. Gonzalez and R. Wynants for their technical support. We thank G. Aerts of CEA/Saclay for the calculation of the weighting functions.

[1] U. Ratzel, C. Arlandini, F. Käppeler, A. Couture, M. Wiescher, R. Reifarth, R. Gallino, A. Mengoni, and C. Travaglio, Phys. Rev. C **70**, 065803 (2004).
[2] Z. Y. Bao, H. Beer, F. Käppeler, F. Voss, and K. Wisshak, At. Data Nucl. Data Tables **76**, 70 (2000).
[3] B. J. Allen, R. L. Macklin, R. R. Winters, and C. Y. Fu, Phys. Rev. C **8**, 1504 (1973).
[4] M. Mizumoto, S. Raman, R. L. Macklin, G. G. Slaughter, J. A. Harvey, and J. H. Hamilton, Phys. Rev. C **19**, 335 (1979).

[5] A. R. de L. Musgrove and R. L. Macklin, EXFOR data library entry: 30386, AAEC/PR46, Australian Atomic Energy Commission, p. 16 (1980).

[6] C. H. M. Broeders and I. Broeders, IAEA-TECDOC-1356 pp. 215–227 (2000).

[7] A. Herrera-Martinez, M. Dahlfors, Y. Kadi, and G. T. Parks, in *Proceedings of the International Workshop on Nuclear Data for the Transmutation of Nuclear Waste*, edited by A. Kelic and K.-H. Schmidt (GSI, Darmstadt, 2003).

[8] http://www-nds.iaea.org/RIPL-2/.

[9] D. J. Horen, J. A. Harvey, and N. W. Hill, Phys. Rev. C **20**, 478 (1979).

[10] D. J. Horen, J. A. Harvey, and N. W. Hill, Phys. Rev. C **24**, 1961 (1981).

[11] *Experimental nuclear reaction data (EXFOR / CSISRS),* see also http://www.nea.fr/html/dbdata/x4/.

[12] C. Domingo-Pardo *et al*., submitted to Phys. Rev. C.

[13] A. Borella, G. Aerts, F. Gunsiing, M. Moxon, P. Schillebeeckx, and R. Wynants, Nucl. Instrum. Methods A **577**, 626 (2007).

[14] A. Borella, Ph.D. thesis, Ghent University (2005).

[15] M. Flaska, A. Borella, D. Lathouwers, L. C. Mihailescu, W. Mondelaers, A. J. M. Plompen, H. van Dam, and T. H. J. J. van der Hagen, Nucl. Instrum. Methods A **531**, 394 (2004).

[16] D. Tronc, J. M. Salomé, and K. H. Böckhoff, Nucl. Instrum. Methods A **228**, 217 (1985).

[17] J. N. Wilson, B. Haas, S. Boyer, D. Dassie, G. Barreau, M. Aiche, S. Czajkowski, C. Grosjean, and A. Guiral, Nucl. Instrum. Methods A **511**, 388 (2003).

[18] E. Wattecamps, in *Nuclear Data Standards for Nuclear Measurements*, edited by H. Condé (NEA/OECD, Paris, 1992), pp. 27–33.

[19] M. G. Sowerby, in *Nuclear Data Standards for Nuclear Measurements*, edited by H. Condé (NEA/OECD, Paris, 1992), pp. 51–58.

[20] C. Bastian, A. Borella, F. Gunsing, J. Heyse, S. Kopecky, G. Noguere, P. Siegler, and P. Schillebeeckx, in *Proceedings of the American Nuclear Society's Topical Meeting on Reactor Physics, Vancouver, BC, Canada, September 10–14,* 2006.

[21] M. C. Moxon and J. B. Brisland, Technical Report AEA-INTEC-0630, AEA Technology (1991).

[22] A. Brusegan, G. Noguère, and F. Gunsing, J. Nucl. Sci. Technol. **S2**, 685 (2002).

[23] K. Volev, A. Brusegan, P. Schillebeeckx, P. Siegler, N. Koyumdjieva, N. Janeva, A. Lukyanov, and L. Leal, in *Proceedings of Workshop on Neutron Measurements, Evaluations and Applications-2*, edited by A. J. M. Plompen (EC-JRC-IRMM, Geel, 2004), pp. 164–167.

[24] F. G. Perey, in *Proceedings of the International Conference on Nuclear Data for Basic and Applied Science*, edited by P. G. Young, R. E. Brown, G. F. Auchampaugh, P. W. Lisowksi, and L. Stewart (LANL, Los Alamos, 1985), pp. 1523–1528.

[25] S. F. Mughabghab, *Neutron Cross Sections: Neutron Resonance Parameter and Thermal Cross Sections, Vol. 1, Pat B: $Z = 61 - 100$* (Academic Press, New York, 1984).

[26] A. Borella, A. Brusegan, M. Moxon, G. Aerts, F. Gunsing, P. Siegler, and P. Schillebeeckx, in *Proceedings of the International Conference on Nuclear Data for Science and Technology*, edited by R. C. Haight, M. B. Chadwick, T. Kawano, and P. Talou (LANL, Los Alamos, 2004), pp. 1539–1542.

[27] J. Briesmeister, Technical Report LA-13709-M, Los Alamos National Laboratory (2000).

[28] C. Domingo-Pardo *et al.* (n_TOF Collaboration), Phys. Rev. C **74**, 025807 (2006).

[29] R. L. Macklin and R. R. Winters, Nucl. Sci. Eng. **78**, 110 (1981).

[30] J. A. Biggerstaf, J. R. Bird, J. H. Gibbons, and W. M. Good, Phys. Rev. **154**, 1136 (1967).

[31] M. Kadi, P. E. Garrett, M. Yeh, S. W. Yates, T. Belgya, A. M. Oros-Peusquens, and K. Heyde, Phys. Rev. C **61**, 034307 (2000).

[32] *EXFOR entry number 22921*.

[33] A. Ioffe, O. Ermakov, I. Karpikhin, P. Krupchitsky, P. Mikula, P. Lukas, and M. Vrana, Eur. Phys. J. A **7**, 197 (2000).

[34] L. Köster and K. Knopf, Z. Phys. A **338**, 233 (1991).

[35] J. C. Blackmon, S. Raman, J. K. Dickens, R. M. Lindstrom, R. L. Paul, and J. E. Lynn, Phys. Rev. C **65**, 045801 (2002).

[36] C. Coceva, in *Nuclear Data Standards for Nuclear Measurements*, edited by H. Condé (NEA/OECD, Paris, 1992), pp. 83–87.

[37] M. B. Chadwick, P. Obložinský, M. Herman *et al*., Nucl. Data Sheets **107**, 2931 (2006).

[38] S. F. Mughabghab, *Atlas of Neutron Resonances, Resonance Parameters and Thermal Cross Sections $Z = 1$–100* (Elsevier, Amsterdam, 2006).

[39] D. J. Horen, R. L. Macklin, J. A. Harvey, and N. W. Hill, Phys. Rev. C **29**, 2126 (1984).

[40] M. Divadeenam and W. P. Beres, in *Statistical Properties of Nuclei*, edited by J. B. Garg (Plenum Press, New York London, 1972), pp. 579–587.

[41] V. G. Soloviev, C. Stoyanov, and V. V. Voronov, Nucl. Phys. **A399**, 141 (1983).

[42] R. Köhler, J. A. Wartena, H. Weigmann, L. Mewissen, F. Poortmans, J. P. Theobald, and S. Raman, Phys. Rev. C **35**, 1646 (1987).

[43] R. J. Baglan, C. D. Bowman, and B. L. Berman, Phys. Rev. C **3**, 2475 (1971).

[44] B. J. Allen, R. L. Macklin, R. R. Winters, and C. Y. Fu, Phys. Rev. C **7**, 2598 (1973).

[45] L. R. Medsker and H. E. Jackson, Phys. Rev. C **9**, 709 (1974).

[46] R. R. Harvey, J. T. Caldwell, R. L. Bramblett, and S. C. Fultz, Phys. Rev. B **136**, 126 (1964).

[47] N. A. Lone, in *Proceedings of the 3th International Symposium on Neutron Capture Gamma-Ray Spectroscopy and Related Topics*, edited by R. E. Chrien and W. R. Kane (Plenum Press, New York, 1979), pp. 161–180.

[48] J. Kopecky, in *Proceedings of the 4th International Symposium on Neutron Capture Gamma-Ray Spectroscopy and Related Topics*, edited by T. von Egidy, F. Gönnenwein, and B. Maier (Institute of Physics, Bristol, 1981), pp. 426–427.

[49] S. Raman, in *Proceedings of the 4th International Symposium on Neutron Capture Gamma-Ray Spectroscopy and Related Topics*, edited by T. von Egidy, F. Gönnenwein, and B. Maier (Institute of Physics, Bristol, 1981), pp. 426–427.

[50] W. V. Prestwich, M. A. Islam, and T. J. Kennett, Z. Phys. A **315**, 103 (1984).

[51] R. L. Macklin and J. H. Gibbons, Rev. Mod. Phys. **37**, 166 (1965).

[52] H. Beer, F. Voss, and R. R. Winters, Astrophys. J. Supp. Ser. **80**, 403 (1992).

[53] T. Nakagawa, S. Chiba, T. Kajino, and T. Hayakawa, At. Data Nucl. Data Tables **91**, 77 (2005).